PCCP

PAPER

View Article Online
View Journal | View Issue

Cite this: *Phys. Chem. Chem. Phys.*, 2014, **16**, 15866

Variable-composition structural optimization and experimental verification of MnB_3 and MnB_4

Haiyang Niu,[ab] Xing-Qiu Chen,*[a] Weijun Ren,[a] Qiang Zhu,[c] Artem R. Oganov,[cbd] Dianzhong Li[a] and Yiyi Li[a]

Received 27th March 2014,
Accepted 15th May 2014

DOI: 10.1039/c4cp01339e

www.rsc.org/pccp

In combination with variable-composition evolutionary algorithm calculations and first-principles calculations, we have systematically searched for all the stable compounds and their crystal structures in the extensively investigated binary Mn–B system. Our results have uncovered four viable ground-state compounds, with Mn_2B, MnB, and MnB_4, and previously never reported MnB_3 and two metastable compounds, MnB_2 and Mn_3B_4. Our calculations demonstrate that the early characterized *mC*10 structure of MnB_4 showed dynamic instability with large imaginary phonon frequencies and, instead, a new *mP*20 structure is predicted to be stable both dynamically and thermodynamically, with a considerable energy gain and no imaginary phonon frequencies. The new MnB_3 compound crystallizes in the monoclinic *mC*16 structure which lies 3.2 meV per atom below the MnB (*oP*8) ↔ MnB_4 (*mP*20) tie-line at T = 0 K. Furthermore, these proposed phases have been verified by our annealed samples after arc-melting synthesis and corresponding powder XRD measurements.

1 Introduction

The fast development of structural prediction methods[1,2] within the first-principles framework of density functional theory (DFT) has resulted in extremely successful progress, such as material discoveries of a novel boron phase (γ-B_{28}),[3] Li-ion batteries,[4] thermoelectric material,[5] topological insulators,[6] superhard carbon allotropes,[7] and so on. Recently, those methods have been extensively applied to transition metal borides (*i.e.* WB_{3+x},[8–11] CrB_4,[12] ReB_2,[13–16] OsB_2,[17,18] FeB_4,[16,19,20] and CaB_6[21]) due to their promising properties, such as facile synthesis at ambient pressure, superior mechanical properties, and good electrical conductivity. Among them, manganese borides are well known for their interesting mechanical properties and have been extensively studied, both experimentally and theoretically.[22–34]

In an early study,[27] the MnB_4 compound was experimentally demonstrated to crystallize in the *mC*10 structure. This structure is characteristic of the three-dimensional (3D) framework of boron with the interconnected square B_4 unit, which is highly similar to that in the early experimentally proposed *oI*10 structure of CrB_4. Recently, this *mC*10 phase was even predicted to exhibit outstanding mechanical properties with an estimated Vickers hardness as high as 49.9 GPa[32] and high ideal strengths, highlighting its potential application.[33] Interestingly, most recently, the square B_4 unit in the *oI*10 structure of CrB_4 was demonstrated, both theoretically and experimentally, to be incorrect and it spontaneously undergoes a distortion into the low-symmetry *oP*10 phase.[12] Therefore, we also suspected whether or not the previously recognized *mC*10-MnB_4 structure was correct. In addition, a *hP*6 (ReB_2-type) phase has been recently proposed as a ground-state phase of MnB_2[29] and it has been further suggested to be superhard.[30] Even though there have been plenty of studies to synthesize this *hP*6 phase, none of them have succeeded in achieving it.[29,31] We also noted that in a recent experimental investigation[31] an unidentified phase called MnB_x has been proposed, experimentally. Within this context, it is highly desirable to carefully revisit the Mn–B binary system by employing recently developed variable-composition evolutionary calculations within Density Functional Theory (DFT) and some suitable experimental characterizations.

2 Methods

In order to identify ambient-condition stable ground-state compositions and structures of the binary manganese–boron system, we have employed the variable-composition evolutionary algorithm,

[a] *Shenyang National Laboratory for Materials Science, Institute of Metal Research, Chinese Academy of Sciences, Shenyang 110016, China. E-mail: xingqiu.chen@imr.ac.cn; Fax: +86-24-23971429; Tel: +86-24-83970102*
[b] *Moscow Institute of Physics and Technology, 9 Institutskiy Lane, Dolgoprudny City, Moscow Region 141700, Russia*
[c] *Department of Geosciences, Center for Materials by Design, and Institute for Advanced Computational Science, State University of New York, Stony Brook, NY 11794-2100, USA*
[d] *School of Materials Science, Northwestern Polytechnical University, Xian 710072, China*

recently implemented in the USPEX code[1,35–38] in coupling with the first-principles calculations within the framework of density functional theory (the Vienna *Ab initio* Simulation Package VASP)[39,40] for the determinations of the total energies, optimized lattice structures and their corresponding electronic structures. For first-principles calculations we employed an all electron projector augmented wave method and the generated gradient approximation (GGA)[41] for the exchange–correlation energy including the approach of Vosko, Wilk and Nusair for spin-polarized systems,[42] along with a plane-wave cutoff energy of 500 eV and dense Monkhorst–Pack *k*-point meshes[43] (with a reciprocal space resolution of $2\pi \times 0.03$ Å^{-1}). The formation enthalpy of the compound of Mn_xB_y is derived with respect to the ground-state phases of α-B[44] and α-Mn.[45] In addition, for the structural candidates searched by USPEX we further derived phonon dispersions using the finite-displacement approach as implemented in the PHONOPY code[46] to clarify the structural stabilities.

Besides theoretical predictions, we have further performed some necessary experiments. A 20 g sample with the initial atomic ratio of B/Mn = 3 was prepared by repeated arc-melting of electrolytic manganese (from Alfa Aesar, claimed purity 99.997%) and crystalline boron pieces (from Alfa Aesar, claimed purity 99.5%) under an argon atmosphere. Based on the analysis of the phase diagram of the Mn–B system,[22,28] we divided the samples into two groups for different treatments. For No. 1 sample, no heat treatment was adopted after melting. For No. 2 sample, it was sealed in quartz under argon atmosphere first and then annealed in a high temperature furnace for 336 h at 1000 °C. The samples were characterized *via* scanning electron microscope (SEM; HITACHI S-3400N) in the back-scattered electron mode (BSE). Finally, the XRD patterns for the two samples were obtained using a Rigaku diffractometer with Cu Kα irradiation (λ = 1.54056 Å).

3 Results and discussions

3.1 First-principles calculations

According to the latest Mn–B phase diagram,[22] five Mn_2B compounds exist (Mg_2Cu type, *oF*48, *Fddd*;[23,24] Al_2Cu type, *tI*12, *I*4/*mcm*[25]), MnB (CrB type, *oC*8, *Cmcm*; FeB type, *oP*8, *Pnma*[25]), Mn_3B_4 (Ta_3B_4 type, *tP*7, *Immm*[25]), MnB_2 (AlB_2 type, *hP*3, *P*6/*mmm*[26]), and MnB_4 (*mC*10, *C*2/*m*[27]). Among them, MnB_2 is a high-temperature phase which can only be synthesized above 1100 °C,[22] which was recently confirmed again.[34] Fig. 1 compiles the DFT formation enthalpies of compounds searched by the variable-composition evolutionary algorithm in USPEX at *T* = 0 K for the $Mn_{1-x}B_x$ ordered structures. For the most stable ground-state phase, we drawn the convex hull in Fig. 1 connecting α-Mn, Mn_2B (*oF*48), MnB (*oI*14), MnB_3 (*mC*16) and MnB_4 (*mP*20), and α-B. Several aspects can be summarized as follows.

(1) Mn_2B and MnB. In good agreement with the experimental findings,[22–25,47,48] our calculations reproduced successfully the experimentally observed structures and compositions

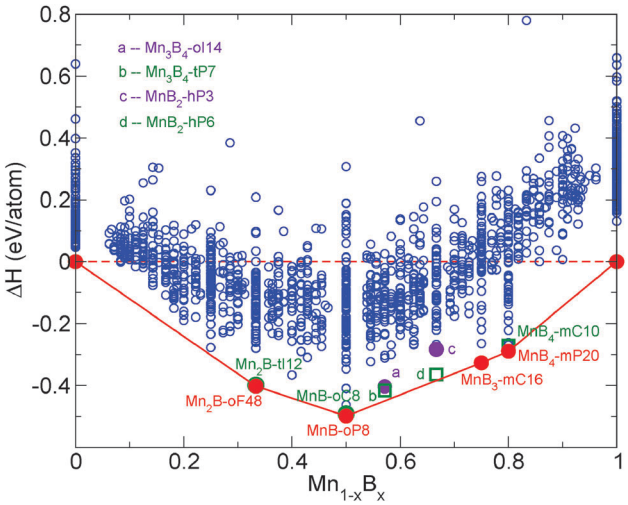

Fig. 1 The derived enthalpies of formation predicted by variable-composition evolutionary computations for the Mn–B system. Every circle represents an individual structure and the most stable ground-state phases (red circles) are connected to form the convex hull.

for both Mn_2B and MnB (*cf.* Table 1). Mn_2B is found to crystallize in the *oF*48 ground-state phase with a derived enthalpy of −0.41 eV per atom lower than the *tI*12 phase, and MnB has an *oP*8 energy-lowest phase, but with an enthalpy of −0.50 eV per atom which is just slightly lower, by 7 meV, than that of the *oC*8 phase. The spin-polarized calculations further revealed that the *oF*48 phase of Mn_2B is non-magnetic. However, both the *oC*8 and *oP*8 phases of MnB are found to be ferromagnetic with the local spin moments of Mn being 1.9 μ_B per atom and 2.0 μ_B per atom, respectively. And our result is in good agreement with previous experimental investigation of the magnetic moment, 1.83 μ_B, of Mn in *oP*8 MnB.[49]

(2) Mn_3B_4 and MnB_2. According to our GGA-level calculations the previously experimentally synthesized Mn_3B_4 and MnB_2 are found to be metastable since their lowest-enthalpy phases are above the convex hull as shown in Fig. 1. For Mn_3B_4, the experimentally reported *oI*14 phase is 0.014 eV per atom less stable in energy than the *tP*7 phase. Interestingly, this *tP*7 phase crystallizes in the tetragonal structure with a space group of $P\bar{4}m2$ (*cf.* Table 1). In particular, it needs to be emphasized that the *oI*14 phase was reported to be antiferromagnetic, in disagreement with our spin-polarized calculations. Our results demonstrate that the antiferromagnetic *oI*14 phase is unstable dynamically because its phonon dispersion exhibits largely imaginary frequencies. In contrast, our results reveal that both the *oI*14 and *oP*7 phases are in the ferromagnetic ordering with the nearly same magnetic moment of 1.9 μ_B per Mn.

For MnB_2, our GGA-level computations found that the most stable phase is the *hP*16 (ReB_2-type) phase with an enthalpy of about −0.36 eV per atom lower than the *hP*3 (AlB_2-type) phase. This result is in good agreement with the previous first-principles calculations.[30,32,34] Our spin-polarized calculations also found that the *hP*16 phase is non-magnetic whereas the *hP*3 phase is antiferromagnetic, with a local spin moment of 2.4 μ_B per Mn, being marginally consistent with the experimental

Table 1 DFT formation enthalpies (ΔH in eV per atom), optimized lattice parameters and Wyckoff sites of the manganese borides searched using USPEX

Phase	Pearson symbol	Prototype	ΔH	Space group cell	Atom	Wyckoff position	x	y	z
α-Mn_2B	*oF*48	Mg_2Cu	−0.4055	*Fddd*	Mn	16f	0.125	0.4531	0.125
				a = 4.1406	Mn	16g	0.125	0.125	0.0438
				b = 7.1489	B	16g	0.125	0.125	0.5011
				c = 14.2770					
β-Mn_2B	*tI*12	Al_2Cu	−0.3993	*I*4/*mcm*	Mn	8h	0.1591	0.6591	0.5
				a = 5.0665					
				b = 5.0665	B	4a	0.0	0.0	0.25
				c = 4.1104					
α-MnB	*oC*8	CrB	−0.4924	*Cmcm*	Mn	4c	0.0	0.3571	0.25
				a = 2.9720					
				b = 7.6151	B	4c	0.0	0.0683	0.25
				c = 2.9599					
β-MnB	*oP*8	FeB	−0.4996	*Pnma*	Mn	4c	0.1746	0.25	0.6232
				a = 5.4587					
				b = 2.9838	B	4c	0.0334	0.25	0.1149
				c = 4.1263					
Mn_3B_4	*oI*14	Ta_3B_4	−0.4035	*Immm*	Mn	2a	0.0	0.0	0.0
				a = 2.9314	Mn	4j	0.5	0.0	0.1826
				b = 3.0020	B	4j	0.0	0.0	0.4321
				c = 12.6771	B	4j	0.5	0.0	0.3542
Mn_3B_4	*tP*7	Mn_3B_4	−0.4162	$P\bar{4}m2$	Mn	1d	0.0	0.0	0.5
				a = 2.9684	Mn	2g	0.0	0.5	0.1283
				b = 2.9684	B	2f	0.5	0.5	0.3651
				c = 6.3734	B	2g	0.0	0.5	0.7849
MnB_2	*hP*3	AlB_2	−0.2831	*P*6/*mmm*	Mn	1a	0.0	0.0	0.0
				a = 2.9868					
				b = 2.9868	B	2d	0.3333	0.6667	0.5
				c = 2.9418					
				γ = 120°					
MnB_2	*hP*6	ReB_2	−0.3648	$P6_3/mmm$	Mn	2c	0.3333	0.6667	0.25
				a = 2.7784					
				b = 2.7784	B	4f	0.3333	0.6667	0.5517
				c = 6.9539					
				γ = 120°					
MnB_3	*mC*16	MnB_3	−0.3268	*C*2/*m*	Mn	4i	0.2899	0.0	0.7958
				a = 7.1372	B	4i	0.0070	0.0	0.7127
				b = 2.8367	B	4i	0.1771	0.0	0.4735
				c = 5.9092	B	4i	0.4275	0.0	0.1194
				β = 90.3629°					
MnB_4	*mC*10		−0.2711	*C*2/*m*	Mn	2a	0.0	0.0	0.0
				a = 5.4946					
				b = 5.3754	B	8j	0.2027	0.3408	0.2026
				c = 2.9532					
				β = 122.51°					
MnB_4	*mP*20		−0.2890	$P2_1/c$	Mn	4e	0.2230	0.4995	0.2706
				a = 5.4717	B	4e	0.1251	0.1805	0.1293
				b = 5.3567	B	4e	0.3422	0.3695	0.8372
				c = 5.4384	B	4e	0.1384	0.3138	0.6357
				β = 114.75°	B	4e	0.3244	0.1304	0.3291

data of 2.6 μ_B[53] obtained by neutron diffraction. Recently, Gou *et al.* performed a GGA + U calculation on MnB_2 and found that the *hP*3 phase is stable over the *hP*16 phase,[34] interpreting the experimental formation of the *hP*3 phase. But, the GGA + U calculations yielded a higher magnetic moment of 3.3 μ_B, much higher than the experimental data.[34] Therefore, one would need to carefully estimate the artificial option of the correlation U effect of the Mn d-states within the DFT framework, which certainly affects its relatively stability. However, to date the lowest-enthalpy non-magnetic *hP*16 phase at the GGA level has been never synthesized.

(3) MnB_4. From Fig. 1 the early experimentally proposed *mC*10 phase[27] is uncovered to be thermodynamically less stable by 0.018 eV per atom than the currently theoretical found *mP*20

phase with the space group of $P2_1/c$ (Table 1). As mentioned above, the *mC*10 phase is built up by an unusual framework of interconnected square B_4 units (Fig. 2a), which is highly similar to the C_4 unit in the tetragonal body-centered allotrope (bct-C_4[54]) of carbon. Clearly, our derived phonon dispersion of this *mC*10 phase demonstrates that it is indeed unstable, dynamically, because significant imaginary phonon frequencies have appeared, as evidenced in Fig. 2c. Interestingly, our calculations uncovered that the real crystal structure of MnB_4 is the *mP*20 phase comprised of the distorted B_4 parallelogram units (Fig. 2b), showing a highly similar version to the most refined *oP*10 phase of CrB_4.[12] The phonon dispersions provide robust evidence of the dynamic stability of the *mP*20 phase, as illustrated in Fig. 2d.

We also noted that the same structure for MnB_4, $P2_1/c$, has been proposed based on first-principles calculations,[50] and confirmed both by a normal-pressure synthesis method,[51] and a high-pressure, high-temperature synthesis technique.[50] Interestingly, both FeB_4 and CrB_4 crystallize in the *oP*10 structure, but the slight distortion of the Mn site further reduces the symmetry of the unit cell of MnB_4 to the monoclinic *mP*20 structure, which can be attributed to Peierls distortion.[50–52]

The spin-polarized calculations further indicate that MnB_4 is non-magnetic. The most recently published experimental work[50] has shown that MnB_4 holds a paramagnetic effective moment of about 1.7 μ_B above 150–200 K, and a sizable effective moment and ferromagnetic spin correlations at 2 K by magnetization measurements. These discrepancies can be mainly explained by the electron localization tendency on the Mn sites.[50] Although by introducing the effect of the on-site Coulomb repulsions *U*, a small ferromagnetic moment about 0.6 μ_B on Mn atoms can be obtained by the LSDA + *U* method,[50] the origin of the ferromagnetic spin correlations is highly puzzling.

(4) MnB_3. Our USPEX searches found a never-observed MnB_3 phase to be thermodynamically stable with respect to the known compounds in Fig. 1 in the well-known Mn–B binary system. As illustrated in Fig. 3a, MnB_3 crystallizes in the *mC*16 (C_2/m) structure (Table 1) and its phonon spectra (Fig. 3b) show no negative frequencies, thereby being stable, both dynamically and thermodynamically. In addition, the spin-polarized calculations show that MnB_3 is non-magnetic.

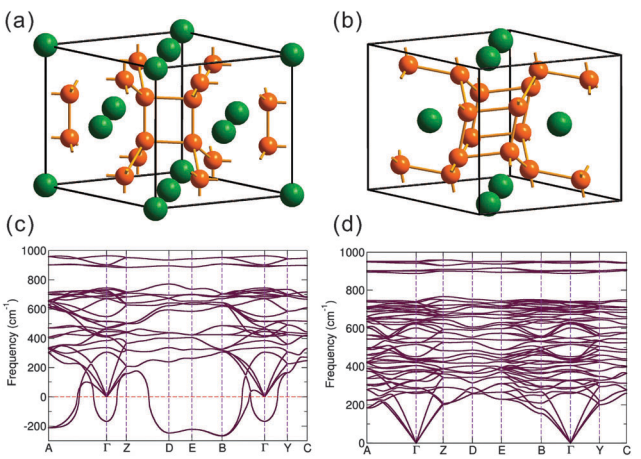

Fig. 2 The crystal structures and their phonon dispersions of MnB_4: (a) the previously experimentally synthesized monoclinic *mC*10 structure,[27] (b) the USPEX searched theoretical monoclinic *mP*20 structure, (c) the derived phonon dispersion of the *mC*10 phase which has been proven to be unstable, mechanically, and (d) the derived phonon dispersion of the *mP*20 phase that is stable, both mechanically and thermodynamically.

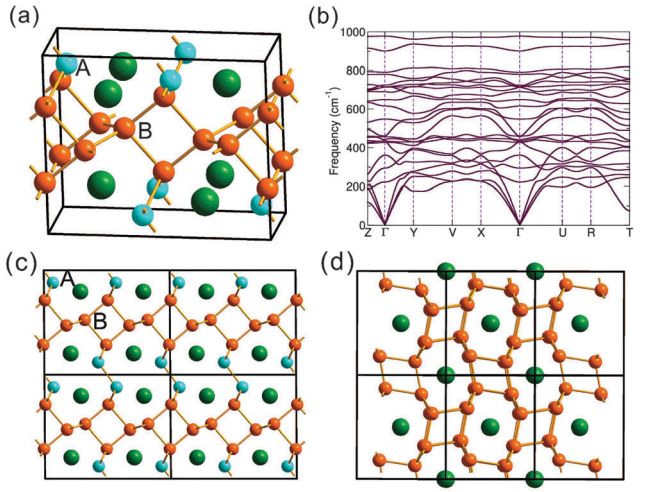

Fig. 3 (a and b) The *mC*16 crystal structure of MnB_3 and its corresponding phonon dispersions, respectively. (c and d) The projections in the 2 × 1 × 2 supercells along the *b*-axis of MnB_3 (*mC*16) and the 2 × 2 × 1 supercells along the (10−1) direction of MnB_4 (*mP*20), respectively. The boron atoms in the *mC*16 phase can be classified into two types, one (marked by B in orange) being four-fold coordinated with its nearest-neighboring (NN) boron atoms and the other one (marked by A in blue) being three-fold bound with its NN boron atoms, whereas the boron atoms are all four-fold coordinated with their NN boron atoms in the *mP*20 phase.

In particular, we would like to stress that the ground-state *mC*16 phase of MnB_3 is indeed closely related to the *mP*20 phase of MnB_4. As evidenced in Fig. 3c and 3d, the projections along the *c*-axis for both MnB_3 and MnB_4 clearly show that the boron framework in MnB_4 is composed of the 4 + 8 membered rings of boron atoms, whereas for MnB_3 the eight-membered boron rings have been broken due to the removal of one boron atom. This fact leaves some boron atoms (marked by A and in blue) in MnB_3 as coordinated by just three other boron atoms, compared with MnB_4 in which each boron atom is four-fold bonded with its nearest-neighboring borons.

During the preparation process of this work, we have also recognized that Van Der Geest and Kolmogorov have generated the largest *ab initio* database for metal borides considering known and new crystal structures identified in selected evolutionary searches using the MAISE package.[55] They also predicted the *mP*20 structure to be the ground state for the MnB_4 composition but did not carry out an evolutionary search for MnB_3. All other findings for the Mn–B system are in excellent agreement.

3.2 Experiments

The experimental powder XRD pattern of the as-cast, No. 1 arc-melting sample is shown in Fig. 4a. It can be seen that the XRD pattern of *hP*3 (AlB_2-type) MnB_2 is in a good agreement with the

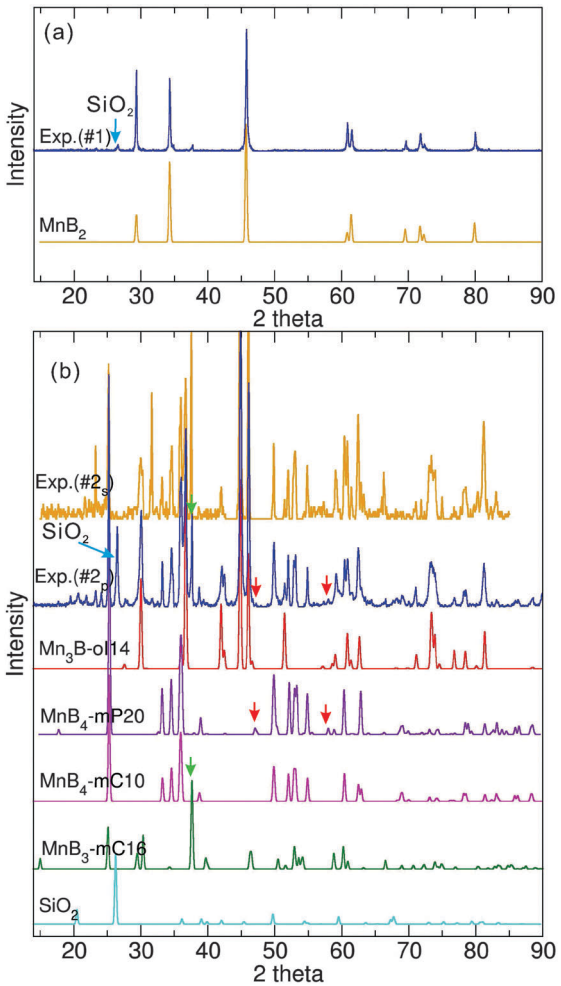

Fig. 4 Experimental and simulated X-ray diffraction patterns of (a) the as-cast No. 1 sample: the experimental XRD pattern *vs.* the theoretical phase of MnB_2, and (b) the annealed No. 2 sample: the experimental pattern (2_s refers to the surface XRD test and 2_p refers to the powder XRD test) along with the theoretical ones of Mn_3B_4 (*hP*3), MnB_4 (*mP*20 and *mC*10), and MnB_3 (*mC*16). The peak at 26.4° corresponds to the impurity of SiO_2.

experimental results, confirming the existence of the *hP*3 phase. Analyzing the microscopic structure as shown in Fig. 5, besides MnB_2 there are still some amorphous borons left in the sample, reflecting well the extra boron in our initial sample with a 3 : 1 B/Mn ratio. It is clear that the boron phase does not contribute obviously to the experimental XRD patterns. Although the *hP*6 phase of MnB_2 is revealed to be a ground-state phase, our experiments did not observe its formation mainly because our samples have been synthesized under high temperature and then quickly quenched in the argon atmosphere. This fact has been already interpreted well by another recent first-principles calculation that suggested the *hP*6 phase indeed becomes thermodynamically unstable above 747 °C by deriving phonon free energies,[29] in accordance with our current experimental synthesis at high temperature.

From the Mn–B binary phase diagram,[22,28] MnB_2 would decompose into Mn_3B_4 and MnB_4 below 1100 °C. In order to reproduce this process, the No. 2 sample was annealed at 1000 °C for 336 h.

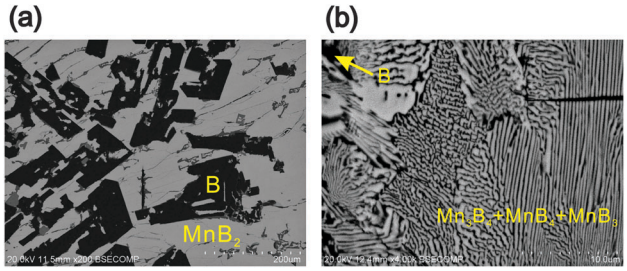

Fig. 5 EBSD micrograph images (a) the as-cast No. 1 sample and (b) the annealed No. 2 sample.

The SEM image shows a typical feature of the eutectoid reaction with the lamellar patterns (Fig. 5). As revealed in the experimental powder XRD patterns, the existence of MnB_4 and Mn_3B_4 has been confirmed. Firstly, our experiments have confirmed the existence of the theoretically proposed *mP*20 phase and excluded the *mP*20 structure that was characterized by the previous XRD experiment.[27] In particular, it needs to be mentioned that the simulated XRD patterns of both stable *mP*20 and unstable *mC*10 phases of MnB_4 are indeed very similar, except for two very tiny extra peaks at 2θ of 47.2 and 58.0° for the *mP*20 phase. As marked by two red arrows in Fig. 4b, the experimental XRD patterns exhibit these two small peaks, thereby providing robust evidence of the appearance of the *mP*20 phase, in agreement with our current prediction. Moreover, from the XRD patterns in Fig. 4b we still find the existing evidence of the never reported MnB_3 (*mC*16) phase. All its theoretical peaks match well, with the experimental ones mostly matching together with those of MnB_4 and, in particular, the strongest peak at 37.8° shows a perfect agreement with the theoretically simulated peak of the *mC*16 phase.

Here, we would like to emphasize that in a recent experimental investigation[31] an unknown MnB_x was proposed based on the XRD peak at 26.4°, which is also precisely what is seen in our experimental patterns for both No. 1 and No. 2 samples (Fig. 4b). However, our analysis demonstrates that this peak at 26.4° originates from the impurity of SiO_2 introduced during the preparation of the powder of the samples polished using an agate mortar and pestle. To clarify this point, we have further performed a surface X-ray diffraction analysis for our No. 2 annealed sample as shown in Fig. 4b, revealing the disappearance of the peak at 26.4°. Therefore, MnB_x defined in ref. 31 can be safely excluded.

4 Mechanical and electronic properties

Furthermore, Table 2 compiles the theoretically derived elastic constants (c_{ij}) of single crystals, the polycrystalline moduli (G, B, and E) according to the Voight–Reuss–Hill averages,[56–58] Poisson's ratio (ν) and the estimated Vickers hardness (H_v) from our recently proposed empirical formula[59–61] for these borides. It has been seen that these borides exhibit high elastic constants and high hardness as well as a low Poisson's ratio, providing evidence that the manganese borides have potentially interesting mechanical

Table 2 Calculated elastic constants (in GPa), bulk modulus B (in GPa), shear modulus G (in GPa), Young's modulus E (in GPa), Poisson's ratio (ν), Puch's modulus ratio (G/B) as well as the estimated Vickers hardness (H_v, in GPa) of the Mn–B system. The calculated bulk (B), shear (G) and Young's moduli (E) are estimated by the Voight–Reuss–Hill averages.[56–58] The Vickers hardness estimates (H_v) are obtained with our proposed formula using the calculated elastic moduli[59,60]

	α-Mn_2B *oF*40	β-Mn_2B *tI*12	α-MnB *oC*8	β-MnB *oP*8	Mn_3B_4 *oI*14	Mn_3B_4 *oP*7	MnB_2 *hP*3	MnB_2 *hP*6	MnB_3 *mC*16	MnB_4 *mS*10	MnB_4 *mP*20
C_{11}	592.7	534.6, 535[b]	389.7	414.4	300.8	341.0	615.4	495.2, 488[b]	333.9	549.3, 540[a]	561.7
C_{22}	564.5		521.9	527.7	432.5				455.1	957.6, 954[a]	871.4
C_{33}	585.8	519.6, 494[b]	498.1	504.8	526.8	426.9	393.6	867.3, 864[b]	468.3	531.4, 531[a]	542.2
C_{44}	138.9	223.9, 219[b]	182.9	215.8	161.7	148.3	122.1	276.4, 276[b]	164.8	238.9, 239[a]	232.0
C_{55}	206.1		215.0	218.4	188.5				305.5	243.6, 245[a]	211.7
C_{66}	158.7	168.0, 168[b]	222.0	175.8	116.4	153.4	223.5	164.1, 158[b]	251.7	170.8, 177[a]	239.6
C_{12}	173.7	230.9, 222[b]	137.5	171.1	263.1	227.0	168.4	167.0, 170[b]	42.0	58.3, 60[a]	93.2
C_{13}	196.9	211.0, 216[b]	167.5	147.5	226.4	234.1	111.7	96.4, 99[b]	176.2	121.8, 126[a]	107.7
C_{23}	196.9		149.3	127.7	166.6				175.4	90.0, 102[a]	84.5
C_{15}									10.5	3.67	4.3
C_{25}									−22.4	14.1	−0.03
C_{35}									49.5	13.9	−13.3
C_{46}									17.8	−7.7	6.4
G	177.0	183.0, 201[b]	182.8	186.0	115.7	108.7	168.6	232.7, 237[b]	185.9	240.9, 274[a]	245.0
B	319.7	321.5, 319[b]	266.2	259.1	280.1	275.7	259.9	281.4, 289[b]	218.0	279.8, 282[a]	277.9
E	448.3	461.4, 498[b]	446.2	450.2	305.2	288.2	415.8	547.2, 559[b]	434.3	561.5, 621[a]	568.1
ν	0.27	0.26, 0.24[b]	0.22	0.21	0.32	0.33	0.23	0.18, 0.18[b]	0.17	0.17, 0.13[a]	0.16
G/B	0.55	0.57, 0.63[b]	0.69	0.72	0.41	0.39	0.65	0.83, 0.82[b]	0.85	0.86, 0.97[a]	0.88
H_v	17.7	18.8	24.1	25.8	8.5	7.5	21.2	35.8	32.3	38.5	40.1
H_{Gao}							16.5[b]	40.3[b]	39.5	49.9[b]	48.7

[a] Ref. 66. [b] Ref. 32.

properties. By varying the boron content from Mn_2B to MnB_4, the elastic constants and hardness change significantly. In particular, the compound MnB_4 exhibits the largest shear modulus (G = 243 GPa), the highest Pugh's modulus ratio ($k = G/B$ = 0.885) and the lowest Poisson's ratio of 0.16, which indicates a typical covalently bonding material.[61,62] The estimated bulk modulus of MnB_4, 277.9 GPa, is in good agreement with the experimental results, 254(9) GPa.[50] The Vickers hardness of MnB_4 is estimated to be as high as 40.1 GPa. Based on the most recently published experimental measurements,[50] the Vickers hardness of MnB_4 has been found to be 37.4 GPa at a load of 9.8 N and 34.6 GPa at 14.7 N, near the threshold of superhardness, which makes MnB_4 a promising high-mechanical-performance material. In comparison with MnB_4, the elastic constant of C_{22} of MnB_3 is just half of its corresponding value, mainly because the 4 + 8 membered rings of boron in MnB_3 are broken by the removal of some boron atoms from MnB_4, as discussed above. As expected, the estimated Vickers hardness (32.3 GPa) of MnB_3 is thus lower by about 20% than that of MnB_4, although MnB_3 is still extremely hard. In addition, it needs to be emphasized that there have been several other theoretical models to derive the Vickers hardness.[63–65] Here, we have attempted to use the model of Gao and co-workers which most fits to covalent and ionic compounds[65] to calculate the Vickers hardness for boron-enriched manganese borides. As illustrated in Table 2, the results are in nice agreement with our current data. However, because in Mn-rich compounds the metallic feature is very strong, it is difficult for Gao's model to derive their hardness.

It is well-known that the three-dimensional network of strong covalent bonds is a basic feature of all known hard materials. The high hardness of MnB_3 (*mC*16) and MnB_4 (*mP*20) is consistent with this. As shown in Fig. 6a, the electron localized function (ELF) highlights a strong 3D covalent framework of boron and

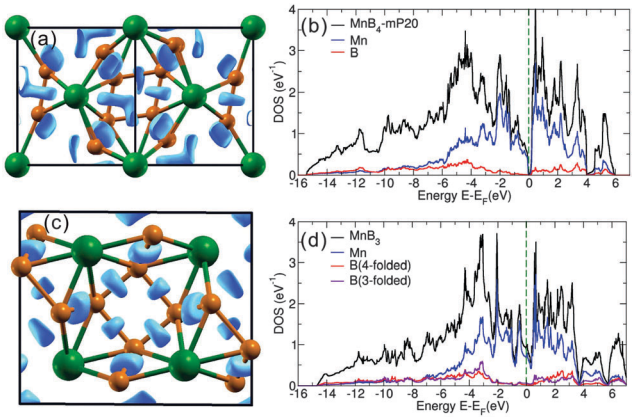

Fig. 6 (a and b) Illustrate the isosurface of the electron localization function (ELF) with an isovalue of 0.75 and the calculated density of states of MnB_4-*mP*20. (c and d) Illustrate the isosurface of the electron localization function (ELF) with an value of 0.75 and the calculated density of states of MnB_3.

each boron atom is covalently bonded with its four nearest-neighboring boron atoms in quasi-sp^3-hybridized configurations with typical covalent charge accumulations along their boron–boron bonds for MnB_4. Nevertheless, besides some four-fold boron atoms in the quasi-sp^3-hybridized configuration in the case of MnB_3 there still exist some three-fold boron atoms in the quasi-sp^2-hybridized configuration (*cf.* Fig. 6c). We have also performed Bader's analysis[67] of MnB_4 and MnB_3. It is interesting to note that for MnB_3 each Mn atom loses the charge of about 0.59*e* on average, whereas for MnB_4 the value is about 0.34*e*. This fact means that for both MnB_3 and MnB_4 the charges are transferred to the B atoms from the Mn atoms. Importantly, the

total quantity of the transferred charges from the Mn atom to B per unit cell for MnB_3 is more than that of MnB_4 ($4 \times 0.59e$ = $2.36e$ for MnB_3 and $4 \times 0.34e$ = $1.36e$ for MnB_4) to help boron form strong boron–boron covalent bonds and stabilize the boron framework. This result implies that the electronic states of Mn in MnB_4 show a little more delocalization, as illustrated in the ELF in Fig. 6. Furthermore, the derived electronic densities of states (DOSs) have been compiled in Fig. 6b and 6d. For both MnB_3 and MnB_4, the DOS profiles show nearly pure-boron regions which correspond to the strong boron–boron covalent bonds. In the energy range from -6 to -2 eV, the relatively strong electronic hybridizations between boron p-like and Mn d-like orbitals have been observed. The non-bonding states basically appear in the energy range from -2 eV to the Fermi level. Interestingly, it can be seen that for MnB_4 the Fermi level sits exactly in the deep pseudo-gap with a nearly zero density, evidencing its electronic stability. However, in the case of MnB_3 the Fermi level is located at the local peak with the DOS value as high as 0.95 states eV^{-1} $atom^{-1}$, resulting in a relatively large electronic specific heat coefficient of $\gamma \approx 3.4$ mJ^{-1} mol^{-1} K^{-2}.

5 Conclusions

In summary, through first-principles calculations and variable-composition evolutionary calculations as well as the relevant experimental synthesis, we have uncovered four viable ground-state compounds, with Mn_2B, MnB, MnB_4 and the previously never reported MnB_3 compositions, and two metastable compounds of MnB_2 and Mn_3B_4. In addition to all experimental observations of those borides, our calculations demonstrate that the early characterized *mC*10 structure of MnB_4 should superseded by the *mP*20 structure predicted and confirmed by our experiment. The previously never observed MnB_3 has been confirmed experimentally to crystallize in the monoclinic *mC*16 structure, in agreement with predictions.

Methodologically, our study highlights the need to re-check the even well-defined known metallic borides, nitrides, and carbides, given the fact both MnB_4 and our recently published CrB_4[12] and WB_{3+x}[8] were characterized inaccurately in the earlier literature. This type of problem is mainly caused by the weak scattering of X-rays for light elements (*i.e.* B, N, C), which become masked by heavier atoms in the compounds, and consequently, powder XRD is almost blind to the lighter elements. Therefore, accurate characterization becomes difficult for those compounds if only based on the powder XRD pattern which has been the most extensively used method. To this end, the universal variable-composition predictor, USPEX, which has performed extremely successfully as shown for this Mn–B system, provides a powerful method to resolve those problems, opening a new horizon for the discovery and characterization of materials.

Acknowledgements

We are grateful for support from the ''Hundred Talents Project'' of Chinese Academy of Sciences and from NSFC of China (Grand Number: 51074151) as well as Beijing Supercomputing Center of CAS (including its Shenyang branch). Financial support from DARPA (Grants No. W31P4Q1310005 and No. W31P4Q1210008), National Science Foundation (EAR-1114313, DMR-1231586), CRDF Global (UKE2-7034-KV-11), Government of the Russian Federation (No. 14.A12.31.0003 and No. W31P4Q1310005) and Russia Ministry of Education and Science (No. 8512) is gratefully acknowledged.

References

1 *Modern Methods of Crystal Structure Prediction*, ed. A. R. Oganov, Wiley, 2011.
2 S. Curtarolo, W. Setywan, G. L. W. Hart, M. Jahnatek, R. V. Chepulskii, R. H. Taylor, S. Wang, J. Xue, K. Yang, O. Levy, M. J. Mehl, H. T. Stokes, D. O. Demchenko and D. Morgan, *Comput. Mater. Sci.*, 2012, **58**, 218–226.
3 A. R. Oganov, J. Chen, C. Gatti, Y. Ma, Y. Ma, C. W. Glass, Z. Liu, T. Yu, O. O. Kurakevych and V. L. Solozhenko, *Nature*, 2009, **457**, 863–867.
4 G. Ceder, *MRS Bull.*, 2010, **35**, 693–701.
5 S. Wang, Z. Wang, W. Setyawan, N. Mingo and S. Curtarolo, *Phys. Rev. X*, 2011, **1**, 021012.
6 K. S. Yang, W. Setyawan, S. D. Wang, M. B. Nardelli and S. Curtarolo, *Nat. Mater.*, 2012, **11**, 614–619.
7 H. Y. Niu, X.-Q. Chen, S. B. Wang, D. Z. Li and Y. Y. Li, *Phys. Rev. Lett.*, 2012, **108**, 135501.
8 X. Y. Cheng, W. Zhang, X.-Q. Chen, H. Y. Niu, P. T. Liu, K. Du, G. Liu, D. Z. Li, H.-M. Cheng, H. Q. Ye and Y. Y. Li, *Appl. Phys. Lett.*, 2013, **103**, 171903.
9 Q. Gu, G. Krauss and W. Steurer, *Adv. Mater.*, 2008, **20**, 3620–3626.
10 R. Mohammadi, A. T. Lech, M. Xie, B. E. Weaver, M. T. Yeung, S. H. Tolbert and R. B. Kaner, *Proc. Natl. Acad. Sci. U. S. A.*, 2011, **108**, 10958–10962.
11 R. Mohammadi, M. Xie, A. T. Lech, C. L. Turner, A. Kavner, S. H. Tolbert and R. B. Kaner, *J. Am. Chem. Soc.*, 2012, **134**, 20660–20668.
12 H. Y. Niu, J. Q. Wang, X.-Q. Chen, D. Z. Li, Y. Y. Li, P. Lazar, R. Podloucky and A. N. Kolmogorov, *Phys. Rev. B: Condens. Matter Mater. Phys.*, 2012, **85**, 144116.
13 H.-Y. Chung, M. B. Weinberger, J. B. Levine, A. Kavner, J.-M. Yang and S. H. Tolbert, *Science*, 2007, **316**, 436–439.
14 J. B. Levine, S. L. Nguyen, H. I. Rasool, J. A. Wright, S. E. Brown and R. B. Kaner, *J. Am. Chem. Soc.*, 2008, **130**, 16953.
15 X.-Q. Chen, C. L. Fu, M. Krčmar and G. S. Painter, *Phys. Rev. Lett.*, 2008, **100**, 196403.
16 A. N. Kolmogorov, S. Shah, E. R. Margine, A. F. Bialon, T. Hammerschmidt and R. Drautz, *Phys. Rev. Lett.*, 2010, **105**, 217003.
17 J. B. Levine, S. H. Tolbert and R. B. Kaner, *Adv. Funct. Mater.*, 2009, **19**, 3519–3533.
18 A. L. Ivanovskii, *Prog. Mater. Sci.*, 2012, **57**, 184–228.
19 A. F. Bialon, T. Hammerschmidt, R. Drautz, S. Shah, E. R. Margine and A. N. Kolmogorov, *Appl. Phys. Lett.*, 2011, **98**, 081901.

20 H. Y. Guo, N. Dubrovinskaia, E. Bykova, A. A. Tsirlin, D. Kasinathan, A. Richter, M. Merlini, M. Hanfland, A. M. Abakumov, D. Batuk, G. V. Tendeloo, Y. Nakajima, A. V. Kolmogorov and L. Dubrovinsky, *Phys. Rev. Lett.*, 2013, **111**, 157002.
21 A. N. Kolmogorov, S. Shah, E. R. Margine, A. K. Kleppe and A. P. Jephcoat, *Phys. Rev. Lett.*, 2012, **109**, 075501.
22 O. Kkamoto, *J. Phase Equilib.*, 1993, **14**, 121–122.
23 B. Aronsson and A. Aselius, *Acta Chem. Scand.*, 1958, **12**, 1476–1480.
24 L.-E. Tergenius, *J. Less Common Met.*, 1981, **82**, 335–340.
25 R. Kiessling, *Acta Chem. Scand.*, 1950, **4**, 146–159.
26 B. Aronsson, *Acta Chem. Scand.*, 1960, **14**, 1414–1418.
27 S. Andersson and J.-O. Carlsson, *Acta Chem. Scand.*, 1970, **24**, 1791–1799.
28 P. K. Liao and K. E. Spear, *Bull. Alloy Phase Diagrams*, 1986, **7**, 543–549.
29 J. Fan, K. Bao, X. L. Jin, X. X. Meng, D. F. Duan, B. B. Liu and T. Cui, *J. Mater. Chem.*, 2012, **22**, 17630–17635.
30 A. Aydin and M. Simsek, *Phys. Rev. B: Condens. Matter Mater. Phys.*, 2009, **80**, 134107.
31 X. X. Meng, K. Bao, P. W. Zhu, Z. He, Q. Tao, J. J. Li, Z. P. Mao and T. Cui, *J. Appl. Phys.*, 2012, **111**, 112616.
32 B. Wang, X. Li, Y. X. Wang and Y. F. Tu, *J. Phys. Chem.*, 2011, **115**, 21429–21435.
33 H. Y. Gou, Z. P. Li, H. Niu, F. M. Gao, J. W. Zhang and R. C. Ewing, *Appl. Phys. Lett.*, 2012, **100**, 111907.
34 H. Y. Gou, G. Steinle-Neumann, E. Bykova, Y. Nakajima, N. Miyajima, Y. Li, S. V. Ovsyannikov, L. S. Dubrovinsky and N. Dubrovinskaia, *Appl. Phys. Lett.*, 2013, **102**, 061906.
35 A. R. Oganov and C. W. Glass, *J. Chem. Phys.*, 2006, **124**, 244704.
36 A. R. Oganov, A. O. Lyakhov and M. Valle, *Acc. Chem. Res.*, 2011, **44**, 227–237.
37 A. O. Lyakhov, A. R. Oganov, H. T. Stokes and Q. Zhu, *Comput. Phys. Commun.*, 2013, **184**, 1172–1182.
38 A. R. Oganov, Y. Ma, A. O. Lyakhov, M. Valle and C. Gatti, *Rev. Mineral. Geochem.*, 2010, **71**, 271–298.
39 G. Kresse and J. Furthmller, *Phys. Rev. B: Condens. Matter*, 1996, **54**, 11169–11186.
40 G. Kresse and J. Furthmller, *Comput. Mater. Sci.*, 1996, **6**, 15–50.
41 J. P. Perdew, K. Burke and M. Ernzerhof, *Phys. Rev. Lett.*, 1996, **77**, 3865–3868.
42 S. H. Vosko, L. Wilk and M. Nusair, *Can. J. Phys.*, 1980, **58**, 1200–1211.
43 H. J. Monkhorst and J. D. Pack, *Phys. Rev. B: Solid State*, 1976, **13**, 5188–5192.
44 G. Will and B. Z. Kiefer, *Z. Anorg. Allg. Chem.*, 2001, **627**, 2100–2104.
45 A. C. Lawson, A. C. Larson, M. C. Aronson, S. Johnson, Z. Fish, P. C. Canfield, J. D. Thompson and R. B. Von Dreele, *J. Appl. Phys.*, 1994, **76**, 7049–7051.
46 A. Togo, F. Oba and I. Tanaka, *Phys. Rev. B: Condens. Matter Mater. Phys.*, 2008, **78**, 134106.
47 T. Kanaizuka, *J. Solid State Chem.*, 1982, **41**, 195–204.
48 G. Papesch, H. Nowotny and F. Bensovsky, *Monatsh. Chem.*, 1973, **104**, 933–942.
49 P. Mohn and D. G. Pettifor, *J. Phys. C: Solid State Phys.*, 1988, **21**, 2829–2839.
50 H. Y. Gou, A. A. Tsirlin, E. Bykova, A. M. Abakumov, G. Van Tendeloo, A. Richter, S. V. Ovsyannikov, A. V. Kurnosov, D. M. Trots, Z. Konôpková, H.-P. Liermann, L. Dubrovinsky and N. Dubrovinskaia, *Phys. Rev. B: Condens. Matter Mater. Phys.*, 2014, **89**, 064108.
51 A. Knappschneider, C. Litterscheild, N. C. George, J. Brgoch, N. Wagner, J. Beck, J. A. Kurzman, R. Seshadri and B. Albert, *Angew. Chem., Int. Ed.*, 2014, **53**, 1684–1688.
52 M. Yang, Y. C. Wang, J. L. Yao, Z. P. Li, J. Zhang, L. L. Wu, H. Li, J. W. Zhang and H. Y. Gou, *J. Solid State Chem.*, 2014, **213**, 52–56.
53 E. Legrand and S. Neov, *Solid State Commun.*, 1972, **10**, 883–885.
54 K. Umenoto, R. M. Wentzcovitch, S. Saito and T. Miyake, *Phys. Rev. Lett.*, 2010, **104**, 125504.
55 A. G. Van Der Geest and A. G. Kolmogorov, *CALPHAD: Comput. Coupling Phase Diagrams Thermochem.*, 2014, **46**, 184–204.
56 W. Voigt, *Lehrburch der Kristallphysik*, Teubner, Leipzig, 1928, pp. 313–315.
57 A. Reuss, *Z. Angew. Math. Mech.*, 1929, **9**, 49–58.
58 R. Hill, *Proc. Phys. Soc., London, Sect. A*, 1952, **65**, 349–354.
59 X.-Q. Chen, H. Y. Niu, D. Z. Li and Y. Y. Li, *Intermetallics*, 2011, **19**, 1275–1281.
60 X.-Q. Chen, H. Y. Niu, C. Franchini, D. Z. Li and Y. Y. Li, *Phys. Rev. B: Condens. Matter Mater. Phys.*, 2011, **84**, 121405.
61 H. Y. Niu, X.-Q. Chen, P. T. Liu, W. W. Xing, X. Y. Cheng, D. Z. Li and Y. Y. Li, *Sci. Rep.*, 2012, **2**, 718.
62 S. F. Pugh, *Philos. Mag.*, 1954, **45**, 823–843.
63 A. Simunek and J. Vackar, *Phys. Rev. Lett.*, 2006, **96**, 085501.
64 K. Y. Li, X. T. Wang, F. F. Zhang and D. F. Xue, *Phys. Rev. Lett.*, 2008, **100**, 235504.
65 F. M. Gao, J. L. He, E. D. Wu, S. M. Liu, D. L. Yu, D. C. Li, S. Y. Zhang and Y. J. Tian, *Phys. Rev. Lett.*, 2003, **91**, 015502.
66 W. J. Zhao and B. Xu, *Comput. Mater. Sci.*, 2012, **65**, 372–376.
67 R. F. W. Bader, *Atoms in Molecules. A Quantum Theory*, Oxford University Press, Oxford, 1990.